

MULTIBAND MULTIMODE ARCHED BOW-SHAPED FRACTAL HELIX ANTENNA

Daotie Li* and Junfa Mao

Key Laboratory of Ministry of Education of China for Research and Design of Electromagnetic Compatibility of High Speed Electronic Systems, Shanghai Jiao Tong University, Shanghai 200240, China

Abstract—A novel circular arc fractus named Arched Bow-shaped Fractal Curve (ABFC) is originally proposed. Four ABFCs are connected end-to-end, forming so called Arched Bow-shaped Fractal Loop (ABFL). The loop antenna peculiarly presents multiband multimode characteristics with resonance compression. The normal mode, which is pertinent to the loop area and circumference, is found improved with the iterative procedure. Thus, an eight-turned wire helix of small pitch angle ($\alpha = 3^\circ$) with a circular disc ground called Arched Bow-shaped Fractal Helix (ABFH) antenna is shaped from K_2 ABFLs. It can unprecedentedly operate in multiband of axial and off-axial modes with dual-sensed circular polarizations and high gain. Four matched bands ($|S_{11}| \leq -10$ dB) are obtained within 2 GHz–8 GHz, of which $f_1 = 2.34$ GHz (400 MHz, 17.09%; $G = 10.63$ dBi; RHCP), $f_2 = 4.24$ GHz (770 MHz, 18.16%; $G = 12.43$ dBi; LHCP), $f_3 = 5.48$ GHz (300 MHz, 5.47%; $G = 8.13$ dBi; RHCP), and $f_4 = 6.98$ GHz (960 MHz, 13.75%; $G = 15.89$ dBi; RHCP). The unique multiband multimode property has been theoretically analyzed with illustrations and can be attributed to existence of the fractal boundary, which particularly encloses multiple equivalent loops with considerable areas. These peculiarities make K_2 ABFH antenna a very attractive candidate for multiband circularly polarized antennas, especially for space applications, such as spacecrafts communication, remote sensing, and telemetry, where reduction of quantity, height and weight of antennas are urgently wanted. It can also be configured into large array for higher gain service like radars and radio astronomy.

Received 9 May 2013, Accepted 22 June 2013, Scheduled 9 July 2013

* Corresponding author: Daotie Li (maplebirchpaeony@yahoo.com.cn).

1. INTRODUCTION

Maxwell Equations can be used to explain all macro electromagnetic phenomena. The equations indicate that all electromagnetism are temporal-spatial problems. As one of the most important applications of Electromagnetics, antenna embodies the viewpoint very well. It is a spatial electromagnetic problem, which is closely correlated with the geometry, materials, and space environment. Unfortunately, there are usually no definite analytical expressions for precise calculation of the problem. Especially, fractal-shaped antenna is just such a typical type, of which performance is highly dependent upon the geometry. In essence, multiband and miniaturization of a fractal antenna are tightly related to its geometrical characteristics of self-similarity and space-filling, respectively. Fractal antenna is a breakthrough of antenna theory and technology in recent years. It had drawn much attention since it was formally put forth by Cohen [1, 2] 12 years after Mandelbrot established Fractal Geometry in 1983 [3]. Many particular attributes had been discovered for fractal antennas during extensive researches and applications in the past years [4–8].

Mathematically, fractal or fractus is a highly complicated, irregular or broken geometry [3, 9]. Just as its name implies, it consists of similar-shaped or affine-transformed pieces of different scales, which usually cannot be represented with a continuous function. With these exquisite and self-similar structures, a fractal antenna can yield similar, diversiform even optimum current distribution. So, it might have better radiation properties than Euclidean counterparts. So far, almost all fractal antennas utilizing fractal geometries that consist of straight segments, such as Koch curve series [10–12], Minkowski curve [13], Hilbert/Peano curve [14–17] or linearly-edged blocks like Sierpinski Carpet series [18–22]. Naturally, we conceive the idea of fabricating a fractal with curved elements, such as circular or elliptical arc with the hope of further enhancing the antenna's performances, like bandwidth, reflection coefficient, directivity, gain, and polarization.

Cylindrical helix antenna (CHA) was invented by Kraus in 1946 [23–25]. It has two operation modes of circular polarization: normal mode [26] and axial mode. The former is narrow band and the latter is wideband. Polarization sense of both modes is accordant with winding direction of the helix. CHA has been used for various applications like FM radio receiver, satellite communications, GPS [27], electronic reconnaissance and radio astronomy. In principle, CHA is equivalent to a series of identical loop antennas and dipole antennas cascaded one by one. Intuitively, geometry of the loops should bear crucial influence on performance of the antenna. With circular

equivalent loops, CHA has approximately consistent impedance and radiation properties within a broad band, whose perimeter-to-wavelength ratio ranges from $3/4$ to $4/3$ [28]. While the loops have other arbitrary Euclidean geometry like congruent triangle, square, and regular polygon, CHA also presents the wideband trait. And if the loop radius changes continuously, an ultra-wideband will be obtained, such as conical helix antenna [29] and spherical helix antenna. However, it's difficult to obtain multiband helix antenna through coalescing several loops of different radii in series. Heretofore, we would naturally conceive the idea of creating a multiband helix with fractal geometry. Unluckily, it's quite difficult to fancy out a loop with fractal contour and considerable area for a helix antenna. For example, Minkowski Loop [30] is not a good candidate for helix antenna owing to its diminishing area with iteration procedure.

In this paper, we originally propose a novel circularly arched bow-shaped fractal curve and construct a loop with four such fractal curves cascaded end-to-end. For convenience and simplicity, full names of the curve and the loop are written as ABFC and ABFL respectively. We modeled and simulated ABFL of each iterative with Ansoft HFSSTM v.13. Simulation results indicate that electromagnetic properties of the fractal loop are tightly associated with its geometrical characteristics. Then, we designed and fabricated a circularly arched bow-shaped fractal helix (ABFH) antenna from 2-iterated ABFL. Good agreement is acquired from simulation and measurement. Quad-bands, which comprise dual senses of circular polarization and axial/off-axial modes with high gain, are obtained within band 2 GHz–8 GHz. In these bands, AR (Axial Ratio) has low level (≤ 2 dB) and good flatness (≤ 0.05 dB) both in frequency and space. Compared with CHA (K_0 ABFH), K_2 ABFH has a little higher frequency, smaller bandwidth, and comparable radiation properties at fundamental resonance f_1 ; small pitch angle and more geometrical complexity. The peculiarities manifest circularly curved fractal's superiority and ingenious potentiality in performance enhancement of antennas. Meanwhile, these advantages make K_2 ABFH a very attractive candidate for multiband circular polarization applications, such as spacecraft-to-ground-station communications, where several helices for separate bands can be superseded by such one helix. By this way, quantity and weight of antennas, which are significant to spacecrafts, will be reduced greatly.

2. THE ABFC AND ABFL

A fractal-shaped antenna, no matter comprises a fractal curve or a 2-D Euclidean sheet with or without such a fractal edge or side, manifests multiband with shrunk dimension. So, conceiving of fractal curve is a foremost task for developing fractal antennas. The iteration procedure of the proposed fractal curve begins with a circle initiator K_0 of radius $d_0 = 0.5 \cdot L_0 = 15.5$ mm. Then, K_0 changes into K_1 by replacing its four quarter-arcs with four circular arcs of $1.5 \cdot \pi$ radian and radius $d_1 = d_0/3$ then cascaded end-to-end with another four arc segments of $1 \cdot \pi$ radian and the same radius. From K_2 iteration on, the procedure is implemented both on iterative arcs and connecting arcs. The coalescing way must ensure smooth transition of all the circular arcs with identical radii of $d_i = d_0/3^i$. The procedure proceeds to form the ABFC and ABFL of each iterative. The K_i -iterated fractal curves are circumscribed by a common contour square with side length of $L_0 = 2 \cdot d_0 = 31$ mm, as shown in Figure 1. For better explanation of ABFL's traits, Minkowski Loop (ML), which derives from square Koch curve, is also presented for comparison. Here, K_i ($i = 1, 2, \dots, n$) denotes the iterative sequence for convenience. The ABFL and ML are modeled with Ansoft HFSSTM v.13. All shape parameters have close relationship during iterative, as depicted in Formulas (1)–(15) in Appendix A.

As depicted in Figures 1(a)–(d), geometrical difference between ABFL and ML is great. First, initiator of ABFL and ML is a circle and a square respectively. Second, inner loop of ABFL and ML extends outwards and dents inwards separately. The relationships between circumference l_i and area A_i of the loops and iteration K_i are illustrated in Figure 2.

As depicted in Figure 2, enclosed area A_i and A'_i diminish into zero as the fractal contours l_i and l'_i approach infinitude when K_i grows infinitely. For distinct showing discrepancies among these curves, only $K_i \leq 5$ are presented. A'_i has larger initial value than A_i , but it decreases more quickly and gets smaller than A_i when $K_i \geq 2$, which means ML encircles fewer area than ABFL in large iteration. In contrast, l'_i also has bigger initial value than l_i , but it increases more slowly and becomes smaller than l_i when $K_i \geq 18$, which means ML contains shorter circumference than ABFL in high iteration. Consequentially, there will be some electrical discrepancy between the two loops. When $K_i > 5$, values of l_i and l'_i can be calculated from Equations (5) and (7) in the appendix.

Radius r_i (or width w_i) of the two loop wires (or stripes) of each

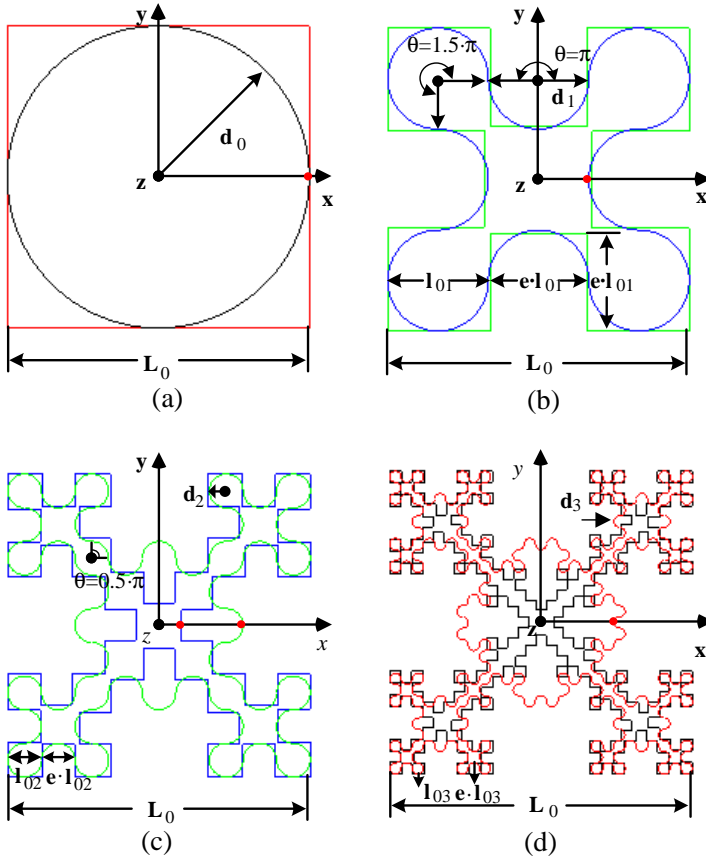


Figure 1. K_i ABFL vs. ML (red, green, blue, and black denotes K_3, K_2, K_1, K_0 of ABFL and black, blue, green, and red denotes K_3, K_2, K_1, K_0 of ML; red spot-feed gap of $g = 0.025$ mm). (a) K_0 (black-ABFL, red-ML). (b) K_1 (blue-ABFL, green-ML). (c) K_2 (green-ABFL, blue-ML). (d) K_3 (red-ABFL, black-ML).

iterative is:

$$r_i | w_i = \frac{r_0 | w_0}{2^{i-1}} \quad (i = 1, 2, \dots, n; \quad r_0 | w_0 = 0.375 \text{ mm}) \quad (1)$$

Form Formula (1) and Figure 1, we can see radius/width of wire/strip decreases with iterative number K_i . And this is the main reason why the maximum iterative time of a fractal wire or stripe antenna is usually chosen as a small natural number, like 2 to 5 times at most, or else the fractal wire or stripe will be self-overlapped

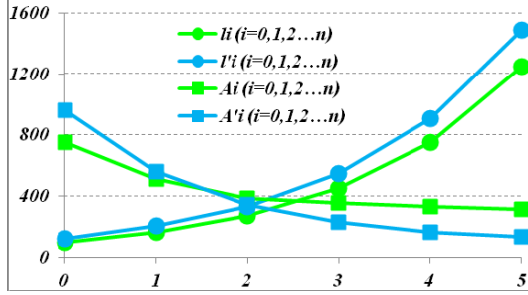


Figure 2. l_i , A_i vs. K_i ($e = 0.95$; green-ABFL, cyan-ML; circle marked- l_i , box-marked- A_i).

or infinitesimal [10, 14]. Of course, the radius relationship between iterative doesn't have the only form like Formula (1), but no matter what form it is, radius surely diminishes with iterative.

3. SIMULATION AND DISCUSSION OF ABFL ANTENNAS

3.1. Simulation of ABFL Antennas

Electrical properties of a fractal antenna can be revealed from its geometrical traits in ideal circumstances. CHA can be analyzed through the equivalent loops, so ABFL antenna will be evaluated from fractal electrical property of the K_0 – K_3 ABFL antenna in free space without matching. For displaying discrepancy of ABFL and ML, K_2 ML is chosen for comparison. Radii of the loop and copper wire are $d_i = d_0/3^i$ and $r_i = r_0/2^i$ ($i = 0, 1, 2, 3$; $d_0 = 15.5$ mm; $r_0 = 0.375$ mm), respectively. The fractal loops are fed with a fixed gap of $g = 0.025$ mm centered at the starting points in $+X$ -axis, as shown in Figure 1, and analyzed with FEM (Finite Element Method) solver of Ansoft HFSSTM v.13 in band 1 GHz–16 GHz. For perfect matching, the impedance of resonance f_{ij} (i – K_i , j – j th resonant frequency of K_i) is chosen as port impedance, so that electrical properties of the fractal loops can be better unveiled. During iteration, ABFLs show distinct fractal electrical properties such as input impedance Z_{in} , bandwidth BW and radiation pattern G , as shown in Figures 3–8. The resonant properties are summarized in Table 1.

Table 1. Simulated resonant properties of K_i ABFL and K_2 ML antennas.

K_0	f_i (GHz)	f_1	f_2		
		3.383	6.791		
	$\delta_n = f_{n+1}/f_n$	-	2.01		
	R_{in} (Ω)	<u>152.25</u>	<u>237.69</u>		
	BW (MHz)	560, 16.56%	1040, 15.31%		
	Gain (dBi)	3.38	4.18		
K_1	f_i (GHz)	f_1	f_2	f_3	
		2.135	3.776	7.63	
	$\delta_n = f_{n+1}/f_n$	-	1.77	2.02	
	R_{in} (Ω)	59.76	86.45	<u>98.12</u>	
	BW (MHz)	108, 5.06%	125, 3.31%	260, 3.35%	
	Gain (dBi)	2.54	3.89	4.94	
K_2	f_i (GHz)	f_1	f_2	f_3	
		1.593	2.835	6.715	
	$\delta_n = f_{n+1}/f_n$	-	1.78	2.37	
	R_{in} (Ω)	37.25	30.86	<u>101.24</u>	
	BW (MHz)	40, 2.51%	30, 1.06%	100, 1.49%	
	Gain (dBi)	2.12	3.92	9.14	
K_2 -ML	f_i (GHz)	f_1	f_2	f_3	
		1.316	2.445	5.689	
	$\delta_n = f_{n+1}/f_n$	-	1.86	2.33	
	R_{in} (Ω)	21.694	14.104	<u>175.417</u>	
	BW (MHz)	11.7, 0.89%	9.5, 0.39%	102, 1.79%	
	Gain (dBi)	2.01	3.86	6.80	
K_3	f_i (GHz)	f_1	f_2	f_3	f_4
		1.413	2.492	5.661	11.927
	$\delta_n = f_{n+1}/f_n$	-	1.76	2.27	2.11
	R_{in} (Ω)	29.67	19.47	79.23	<u>154.42</u>
	BW (MHz)	30, 2.12%	45, 1.81%	71, 1.25%	2530, 21.2%
	Gain (dBi)	2.19	4.21	7.83	6.68

(Bold-low resistance, underscored-high resistance).

3.2. Discussion and Conclusions

As shown in Figures 3–4, the input impedance $Z_{in}(f)$ and reactance $X_{in}(f)$ of K_i ABFL and K_2 ML have remarkable multi-resonance

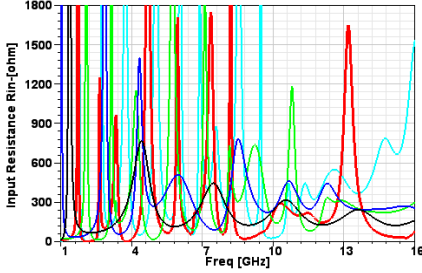


Figure 3. Input resistance $R_{in}(f)$ of K_i ABFL (K_0 -black, K_1 -blue, K_2 -green, K_3 -red, K_2 ML-cyan).

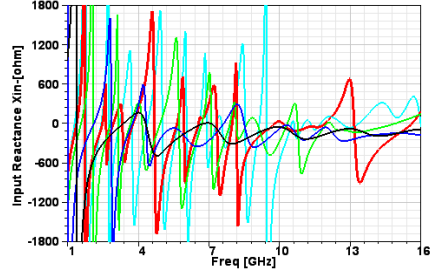


Figure 4. Input reactance $X_{in}(f)$ of K_i ABFL (K_0 -black, K_1 -blue, K_2 -green, K_3 -red, K_2 ML-cyan).

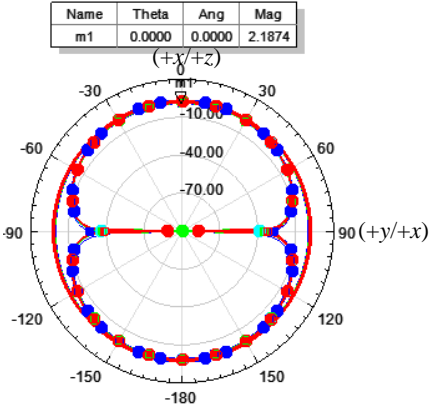


Figure 5. Gain patterns of K_i ABFL and K_2 ML at Mode #1 (bare solid-Phi = 0° , XOZ , H -plane; circle marked solid-Phi = 90° , YOZ , E -plane, box marked solid-Theta = 90° , XOY ; V -polarization; blue- K_1 - f_1 , green- K_2 - f_1 , red- K_3 - f_1 , cyan- K_2 ML- f_1 , as shown in Table 1).

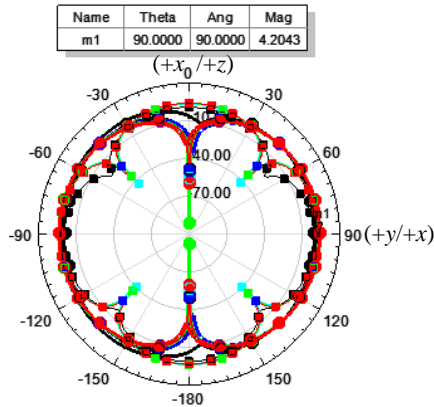


Figure 6. Gain patterns of K_i ABFL and K_2 ML at Mode #2 (bare solid-Phi = 0° , XOZ , H -plane; circle marked solid-Phi = 90° , YOZ , H -plane; box marked solid-Theta = 90° , XOY , E -plane; H -polarization; black- K_0 - f_2 , blue- K_1 - f_2 , green- K_2 - f_2 , red- K_3 - f_2 , cyan- K_2 ML- f_2 , as shown in Table 1).

during iterative process. $R_{in}(f)$ fluctuates between high-low impedances, and $X_{in}(f)$ fluctuates around 0Ω more frequently when K_i grows, which means more resonant frequencies within the band. High and low resistances emerge alternately as reactance swings between inductance and capacitance quickly. Nevertheless, as shown

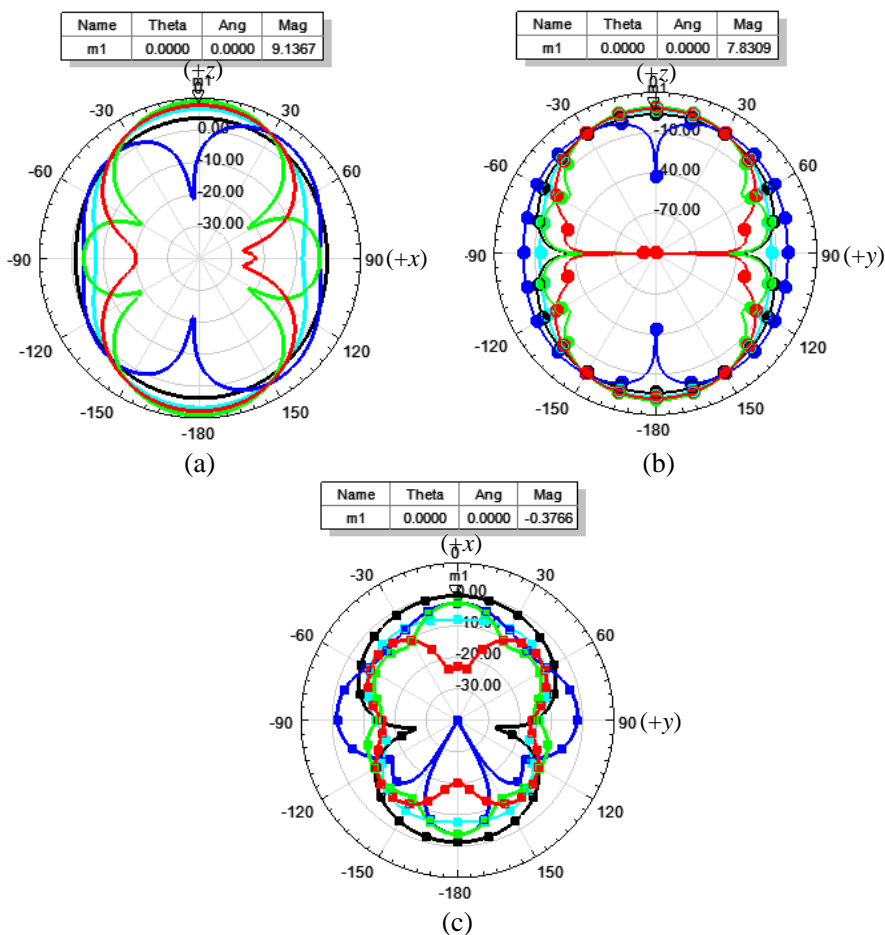


Figure 7. Gain patterns of K_i ABFL and K_2 ML at Mode #3 (bare solid- $\Phi = 0^\circ$, XOZ - H -plane; circle marked solid- $\Phi = 90^\circ$, YOZ , E -plane, box marked solid- $\Theta = 90^\circ$, XOY ; V -polarization; black- K_0 - f_1 , blue- K_1 - f_3 , green- K_2 - f_3 , red- K_3 - f_3 , cyan- K_2 ML- f_3 , as shown in Table 1. (a) $\Phi = 0^\circ$, XOZ . (b) $\Phi = 90^\circ$, YOZ . (c) $\Theta = 90^\circ$, XOY .

in Table 1, number of multi-resonance of K_i never shows the usual relationship of $N = i + 1$ [11,21]. The initiator K_0 has two resonant frequencies, f_1 and f_2 . When it iterates to K_1 , a new lower resonant frequency occurs. The resonance number is unchanged when, K_1 evolves into K_2 , but these resonances all have lower frequency. When K_2 iterates to K_3 , another new resonance emerges in upper band. Impedance difference between K_2 (green) and K_2 ML (cyan) is conspicuous. K_2 ML has lower resonances and larger resistance, reactance in upper band. Resonances f_{ij} of each iterative K_i are categorized by means of putting those who have similar radiation patterns together. Thus, gain patterns of resonant frequencies of identical mode are merged into a pattern for relevance and discrepancy analysis, as depicted in Figures 5–8. In these patterns, bare solid, circle marked, box marked represents $\Phi = 0^\circ$, $\Phi = 90^\circ$, and $\Theta = 90^\circ$ principle cut-planes respectively; and red, green, blue, black, and cyan denotes K_3 , K_2 , K_1 , K_0 , and K_2 ML in sequence. For more distinct display, variable scale range (-100 – $+20$, -40 – $+10$) is chosen for these patterns.

Figure 5 shows that Mode #1 has ideal dipole-like gain pattern with V -polarization, which is omnidirectional in XOZ (H -plane, $\Phi = 0^\circ$) and doughnut-shaped in YOZ (E -plane, $\Phi = 90^\circ$, V -polarization) and XOY ($\Theta = 90^\circ$). Figure 6 shows that Mode #2

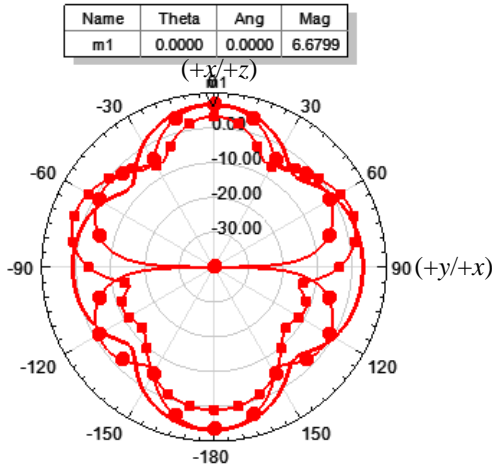


Figure 8. Gain patterns of K_i ABFL at Mode #4 (bare solid- $\Phi = 0^\circ$, XOZ , H -plane; circle marked solid- $\Phi = 90^\circ$, YOZ , E -plane, box marked solid- $\Theta = 90^\circ$, XOY ; V -polarization; red- K_3 - f_4 , as shown in Table 1).

has clove dipole-like radiation pattern with H-polarization, which is doughnut-shaped in XOZ (H -plane, $\Phi = 0^\circ$), YOZ (H -plane, $\Phi = 90^\circ$), and red cross-shaped in XOY (E -plane, $\Theta = 90^\circ$, H -polarization). Figure 7 shows that Mode #3 has bi-directional radiation pattern in normal (Z -axis) with V -polarization, which is peanut-shaped in XOZ (H -plane, $\Phi = 0^\circ$) and YOZ (E -plane, $\Phi = 90^\circ$, V -polarization) with nulls in X/Y -axis ($\Theta = 90^\circ$). Figure 8 shows that Mode #4 also has normal bi-directional radiation patterns but with side lobes in X/Y -axis, which are stub-crossed in XOZ (H -plane, $\Phi = 0^\circ$), cross-shaped in YOZ (E -plane, $\Phi = 90^\circ$, V -polarization) and XOY ($\Theta = 90^\circ$). K_2 ML and K_2 ABFL have almost the same gain patterns in Mode #1, 2. But K_2 ABFL (green) has more ideal peanut-shaped pattern, and its gain is 2.34 dBi larger than K_2 ML (cyan) in Mode #3.

f_1 and f_2 of K_0 ABFL are with Mode #3 and Mode #2; f_1 , f_2 , and f_3 of K_1 , K_2 ABFL, and K_2 ML are with Mode #1, Mode #2, and Mode #3; f_1 , f_2 , f_3 , and f_4 of K_3 ABFL are with Mode #1, Mode #2, Mode #3, and Mode #4. Resonant frequency of Mode #3 first shifts upwards then shifts downwards with K_i , because loop area diminishes but loop circumference grows with K_i . Meanwhile, gain pattern gradually involves into ideal peanut-shaped with K_i . Resonant frequencies of Mode #2 and Mode #1 always shift downwards with K_i due to constant growth of loop circumference. However, they maintain cloven dipole-like and ideal dipole-like gain pattern respectively with K_i .

Surface current density J_s distribution at the resonant frequencies of K_3 ABFL antenna is illustrated in Figures 9–12. Intuitively, we will unveil the fractal traits in essence with the distribution. For better comparison, identical scale is chosen for all plots.

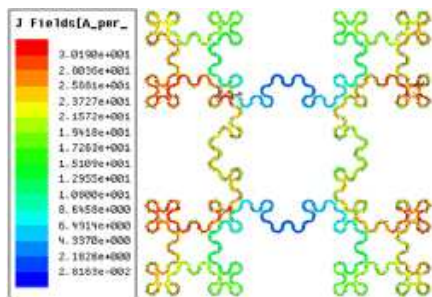


Figure 9. $f_1 = 1.413$ GHz ($1 \cdot \lambda_1$).

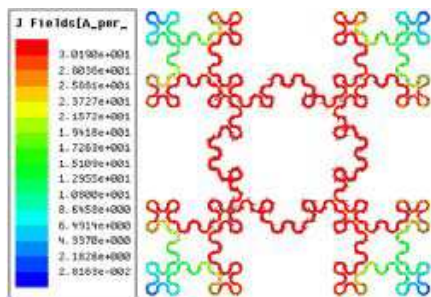


Figure 10. $f_2 = 2.492$ GHz ($2 \cdot \lambda_2$).

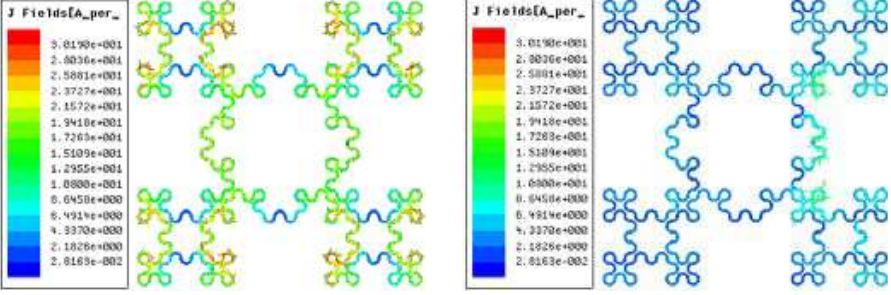


Figure 11. $f_3 = 5.661$ GHz ($5 \cdot \lambda_3$). **Figure 12.** $f_4 = 11.927$ GHz ($15 \cdot \lambda_4$).

From the illustration of J_s in Figures 9–12, we can see that K_3 ABFL antenna operates in integral-timed wavelength, namely the electrical size at f_1 is $1 \cdot \lambda$, at f_2 is $2 \cdot \lambda$, at f_3 is $5 \cdot \lambda$, and at f_4 is $15 \cdot \lambda$. f_1 is dipole-like pattern, f_2 quadrifoliate dipole-like pattern, f_3 normal peanut-shaped pattern, and f_4 normal peanut-shaped pattern with stub-crossed side lobes in X/Y axis. Comparably, all conventional wire electrical loops antenna of various Euclidean shapes only have the normal mode. This phenomenon indicates that ABFL antenna has distinctive peculiarity of multi-resonance and multimode.

We can draw some conclusions from the aforementioned analysis as follows:

- (1) The number of resonant frequencies N_i and iterative times K_i has the following relationship, which is different from other fractal antenna counterparts like Koch/Koch-like [11] dipoles:

$$\begin{aligned}
 N_i &= n_{\max} = \text{mod}(i, 2) + \text{rem}(i, 2) + 2 \quad (i = 0, 1, 2 \dots) \\
 &(\text{mod-modul, rem-remain}; \quad i = k \cdot 2 + k', \quad \text{mod}(i, 2) = k, \\
 &\text{rem}(i, 2) = k', k, k' \in N)
 \end{aligned}$$

- (2) Ratio of adjacent resonant frequencies δ_n can be derived from J_s distribution of K_3 , which is very approximate to fractal scale ratio σ_n when K_i is large enough [11, 21]:

$$\begin{aligned}
 C_{loop} &= N\lambda_{n+1} \cdot \frac{c_0}{f_{n+1}} = N\lambda_n \cdot \frac{c_0}{f_n}; \\
 \lim_{n \rightarrow n_{\max}} \delta_n &= \lim_{n \rightarrow n_{\max}} \frac{f_{n+1}}{f_n} = \lim_{n \rightarrow n_{\max}} \frac{N\lambda_{n+1}}{N\lambda_n} = 3 \approx \sigma_n, \quad (2) \\
 n &= (1, 2, \dots, n_{\max}),
 \end{aligned}$$

where C_{loop} is circumference of the fractal loop, c_0 is light speed in free space; $N\lambda_n$ is wavelength number of f_n on the loop.

- (3) Resonant frequency f_n , resistance R_{in} , and impedance bandwidth of each mode always decreases with iterative times K_i except Mode #3. However, for each iterative case K_i , percentage bandwidth of resonant frequency f_n doesn't monotonously diminish with n .
- (4) Resonant frequency of Mode #3 increases first and then decreases with K_i , because loop area A_i diminishes but loop circumference l_i grows more quickly with K_i . Meanwhile, the gain pattern gradually involves into ideal peanut-shaped with K_i .
- (5) ABFL antenna of each iteration commonly has two fundamental radiation modes, namely Mode #2 (H -polarization) and Mode #3 (V -polarization). When $K_i \geq 1$, an iteratively induced mode, namely Mode #1 (V -polarization) yields; while $K_i \geq 3$, Mode #4 (V -polarization), which is a variant mode of Mode #3 emerges. The larger K_i , the more radiation modes. Gain patterns of Mode #1 and Mode #2 don't significantly change with iteration K_i , but Mode #3 has remarkable improvement in gain patterns with growth of K_i .
- (6) K_i -iterated ($i \geq 1$) ABFL antenna operates in multiband of integral wavelength.
- (7) Compared with K_1 , K_2 , and K_0 counterparts, K_3 ABFL antenna presents 33.82%, 63.31% size shrinkage and 67.34% size increment at Mode #1, Mode #2, and Mode #3 respectively.
- (8) K_2 ABFL (green) has larger bandwidth, more uniform impedances, and higher gain in Mode #1, Mode #2, and Mode #3 than K_2 ML (cyan). However, it has higher resonances than K_2 ML because K_2 ML covers larger area and circumference due to its initiator is bigger than that of ABFL.

Hereunto, we can conclude that ABFL is a more desirable fractal loop than Minkowski Loop due to the fact that it keeps considerable area when perimeter grows infinitely. This property makes it a better choice for multiband and multimode operation, especially for the normal mode, which is relevant to axial mode of helix antenna. Therefore, we bring forth the ideal of designing a high gain multiband helix antenna with this fractal loop in the next Section.

4. K_2 ABFH ANTENNA

4.1. Physical Design of K_2 ABFH Antenna

As discussed in Introduction, helix antenna is a very useful antenna type. However, it is wide but has single band in axial mode operation. If it is made into multiple wideband of this mode, that would bring

a great upgrade in performance and more attractions to applications. Therefore, we preferably modify the ABFC into helix antenna rather than loop antenna. In addition, in view of design and fabrication complexity, we choose $K_i = 2$ as the antenna solution. Thus, a K_2 ABFH antenna is designed and fabricated for the previous assumption. It comprises eight turns of wire-wound K_2 ABFL with a small helix pitch angle θ . Due to periodicity of the helix configuration, equation of a K_2 ABFH can be derived from that of a single turn as follows:

$$\begin{cases} xi(\theta, \varphi) = N_{xi} \cdot d_2 + [d_2 + r_0 \cdot (1 - \theta \cdot \cos \alpha \cdot \tan \beta) \cdot \cos \varphi] \cdot \cos(ai \cdot \theta + bi \cdot \pi) \\ yi(\theta, \varphi) = N_{yi} \cdot d_2 + [d_2 + r_0 \cdot (1 - \theta \cdot \cos \alpha \cdot \tan \beta) \cdot \cos \varphi] \cdot \sin(ai \cdot \theta + bi \cdot \pi) \\ zi(\theta, \varphi) = r_0 \cdot (1 - \theta \cdot \cos \alpha \cdot \tan \beta) \cdot \sin \varphi + \tan \alpha \cdot d_2 \cdot \theta \end{cases}$$

$$\theta \in [\theta_0, \theta_0 + \gamma_i \cdot \pi]; \quad \varphi \in [0, 2 \cdot \pi]; \quad d_2 = \frac{d_0}{3^2} = \frac{17.5}{9} \text{ mm}; \quad r_0 = 0.625 \text{ mm};$$

$$\left(\begin{array}{l} N_{x1} = N_{x2} = N_{x3} = N_{x9} = N_{x10} = N_{x11} = 4; \\ N_{x4} = 6; N_{x5} = N_{x6} = N_{x7} = 8; N_{x12} = 2; N_{x13} = 0; \end{array} \right)$$

$$N_x(12 \cdot k + 1 + i) = -N_x(12 \cdot k + 1 - i);$$

$$N_y[12 \cdot (k - 1) + i] = -N_x[12 \cdot k + 2 - i]$$

$$\left(\begin{array}{l} \gamma_{12 \cdot k+1} = \gamma_{12 \cdot k+2} = \gamma_{12 \cdot k+4} = \gamma_{12 \cdot k+6} = \gamma_{12 \cdot k+8} = \gamma_{12 \cdot k+10} = \gamma_{12 \cdot k+12} = 1; \\ \gamma_{12 \cdot k+3} = \gamma_{12 \cdot k+11} = 0.5; \gamma_{12 \cdot k+5} = \gamma_{12 \cdot k+7} = \gamma_{12 \cdot k+9} = 1.5; \end{array} \right)$$

$$(k = 1, 2, 3; \quad i = 1, 2, \dots, 12)$$

$$ai = (-1)^{i+1}, \quad (i \in \psi = \{1, 2, 3, \dots, 48\});$$

$$bi = \begin{cases} 1, & i \in \phi = \{4, 8, 12, 14, 18, 22, 28, 32, 36, 38, 42, 46\} \\ 0, & i \in \psi - \phi \end{cases}, \quad (3)$$

where θ , θ_0 , and α are winding angle, initial winding angle, and pitch angle of the helix, respectively; φ , β , and r_0 are section azimuth angle, taper angle, and radius of the wire in several; d_0 and d_2 are radius of the initiator and the circular arcs of K_2 ABFL, respectively; $i = 1, 2, \dots, 48$ denotes the i th arc; N_{xi} and N_{yi} are the centre coordinate; a_i and b_i are coefficients of winding direction; γ_i is coefficient of ending angle of the i th arc. From Equation (3), it is clear that ABFH cannot be described with a continuous function but a series of piecewise functions, just as we stated in Section 1. Then, the unit helix is replicated eight times along the axial direction (+ Z -axis) with a turn-to-turn spacing $S = (50 \cdot \pi \cdot d_2) \cdot \tan \alpha$. So, the overall height and total wire length of the K_2 ABFH are $H = 8 \cdot S$ and $L_T = 8 \cdot (S \cdot csc \alpha) = (400 \cdot \pi \cdot d_2) \cdot sec \alpha$, respectively. Likewise, the same solution is adopted in fabrication. First, eight unit wire helices are fabricated with a customized mould, as shown in Figure 13, then soldered end-to-end to form a complete ABFH. The design parameters for the helix antenna are $\alpha = 3^\circ$, $\beta = 0^\circ$,

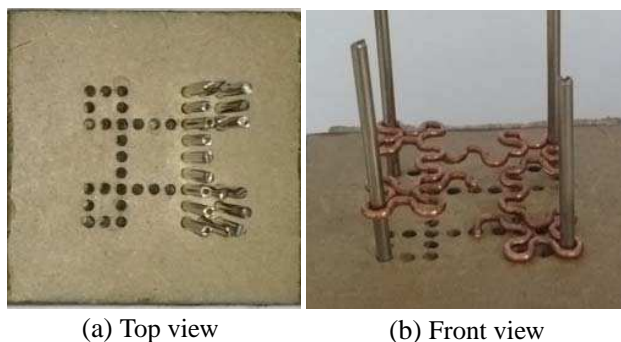


Figure 13. Simple mould for fabrication of K_2 ABFH. ((a) 48 circular holes, which are concentric with the arcs, are drilled in a wood block, then 48 stainless steel posts are inserted into these holes. (b) A unit helix can be fabricated by winding a copper wire of radius $r_0 = 0.625$ mm around these posts).

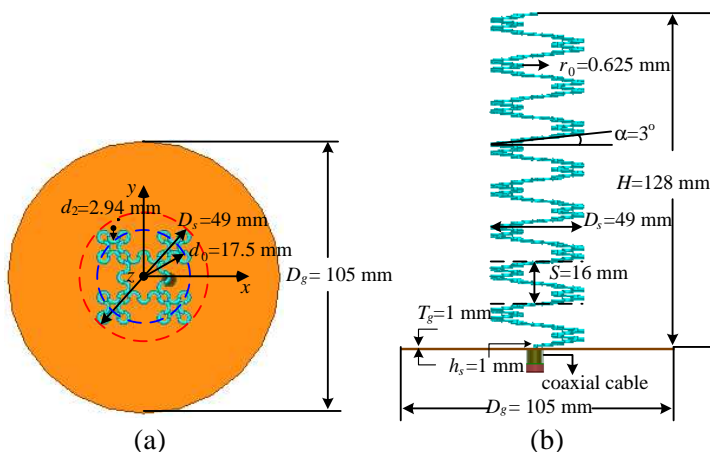


Figure 14. Geometry of K_2 ABFH antenna ((a) Top view, red dash-circumcircle, blue dash-initiator K_0 . (b) Front view, cyan-helix, yellow-ground plate; green-coaxial cable; unit: mm).

$d_0 = 17.5$ mm ($0.12 \cdot \lambda_1$, λ_1 -wavelength of $f_1 = 2.34$ GHz in free space), $d_2 = 2.94$ mm, $r_0 = 0.625$ mm; diameter and thickness of the circular copper ground plate $D_g = 105$ mm ($0.819 \cdot \lambda_1$), $T_g = 1$ mm; distance of the helix above the ground $h_s = 1$ mm. So the circumradius is $D_s = 49$ mm ($0.382 \cdot \lambda_1$); element spacing is $S = 16$ mm ($0.11 \cdot \lambda_1$); overall height is $H = 128$ mm ($0.998 \cdot \lambda_1$), as depicted in Figure 14.

It is directly fed by a $50\ \Omega$ flanged SMA connector with a coaxial stub. The inner conductor of the coaxial stub is soldered with the helix wire and the flange fastened on the ground plate with screw nuts respectively. Owing to considerable weight of copper wire, the helix antenna is sustained in the diagonal corners by four dried bamboo posts of radius $r_p = 2.8\ \text{mm}$ and height $h_p = 138\ \text{mm}$. A photo of the antenna prototype is shown in Figure 15. Because of inaccuracy of the fabrication, geometrical precision of the antenna is not satisfactory.

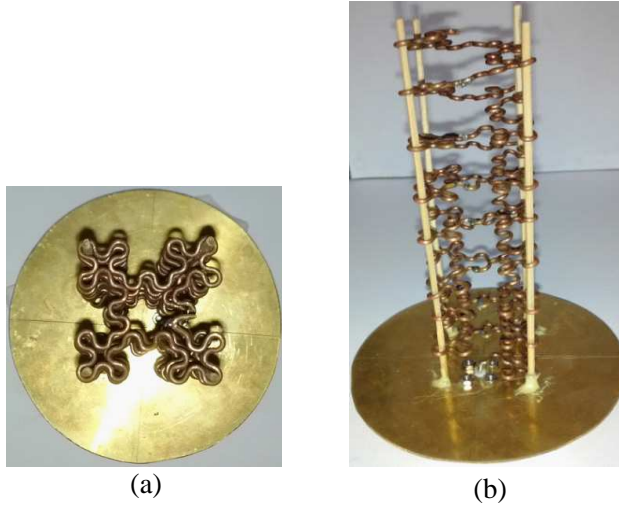


Figure 15. Photos of the prototype of K_2 ABFH antenna (SMA with 4-holed square flange, 4 bamboo posts for support). (a) Top view. (b) Front view.

4.2. Results and Analysis

Full-wave EM analysis was performed with FEM solver of ANSYS HFSSTM v.13 for K_2 ABFH antenna in band 2 GHz–8 GHz. Then, the antenna's prototype was measured for reflection coefficient $|S_{11}|$ and gain patterns in an in-house anechoic chamber. Gain by contrast, peculiarity and superiority of K_2 ABFH antenna will reveal themselves to CHA (K_0 ABFH) with comparison. So, identical simulation analysis is also made for K_0 ABFH antenna, which has the same helix parameters ($r_0 = 0.625\ \text{mm}$, $d_0 = 17.5\ \text{mm}$, $\alpha = 3^\circ$, $N = 8$, $H = 128\ \text{mm}$, $h_s = 1\ \text{mm}$) and ground configuration ($D_g = 105\ \text{mm}$, $T_g = 1\ \text{mm}$). The simulated and measured results of K_2 and K_0 are merged into corresponding plots for discrepancy comparison and redundancy

avoidance. In these plots, red, black, blue denote simulated, measured results of K_2 , and simulated results of K_0 in sequence, as shown in Figures 16, 17 and Figures 19–29.

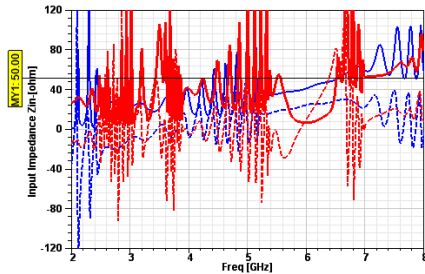


Figure 16. Simulated input impedance Z_{in} of K_i ABFH antenna (red- K_2 , blue- K_0 ; solid- R_{in} , dash- X_{in}).

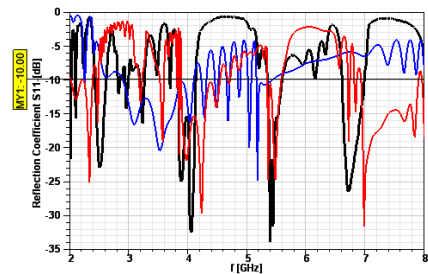


Figure 17. Reflection coefficient $|S_{11}|$ of K_i ABFH antenna (red-simulated of K_2 , black-measured of K_2 , blue-simulated of K_0 at $25\ \Omega$ port impedance).

Multi-resonance property manifests itself remarkably in input impedance Z_{in} . Low and high resonant impedances emerge alternately, as shown in Figure 16. The low impedances (solid- $R_{in} = 35\ \Omega$ – $65\ \Omega$, dash- $X_{in} = -20\ \Omega$ – $+20\ \Omega$) are very approximate to $50\ \Omega$ in quad-bands, which means four matched bands can be obtained easily with $50\ \Omega$ coaxial feeding. Compared with the empirical formula $Z_{in} = R_{in} \approx 140 \cdot C_\lambda$ given by Kraus [24] for a side-fed CHA, K_2 ABFH antenna has lower value due to impedance transformation of fractal geometry and coaxial cable. Z_{in} can be further tuned to $50\ \Omega$ with an extra quarter wavelength of impedance transformer beneath the ground plate or tapering initial segment of the fractal helix wire. Accordingly, $|S_{11}|$ presents quad-bands ($|S_{11}| \leq -10\ \text{dB}$), of which $f_1 = 2.34\ \text{GHz}$ (S -band, $2.02\ \text{GHz}$ – $2.42\ \text{GHz}$, $\text{BW} = 400\ \text{MHz}$, 17.09%), $f_2 = 4.24\ \text{GHz}$ (C -band, $3.81\ \text{GHz}$ – $4.58\ \text{GHz}$, $\text{BW} = 770\ \text{MHz}$, 18.16%), $f_3 = 5.48\ \text{GHz}$ (C -band, $5.35\ \text{GHz}$ – $5.65\ \text{GHz}$, $\text{BW} = 300\ \text{MHz}$, 5.47%), and $f_4 = 6.98\ \text{GHz}$ (C -band, $6.93\ \text{GHz}$ – $7.89\ \text{GHz}$, $\text{BW} = 960\ \text{MHz}$, 13.75%), as shown in Figure 17 and Table 2. For convenience, the quad-band denotes band #1, band #2, band #3, and band #4 separately. Comparably, the simulated (red) and measured (black) results of $|S_{11}|$ are largely accordant with each other though the latter shows narrower bandwidth and conspicuous shifting. This could be mainly imputed to the fabrication tolerance owing to the crude mould and process, as well as inherent error of simulation and the measurement systems. In contrast, K_0 ABFH gets close to $50\ \Omega$ in a single band, so it

has only one matched band but with larger width ($f_c = 3.5$ GHz, 2.91 GHz–4.13 GHz, BW = 1200 MHz, 34.26%). The bandwidth can also be further widened out with those methods proposed for K_2 ABFH antenna.

The multi-resonance properties of K_2 ABFH antenna are summarized in Table 2 for highlighting the fractal features.

Table 2. Resonant properties of K_2 ABFH antenna.

	Item	f_1	f_2	f_3	f_4
f_i (GHz)	sim	2.34	4.24	5.48	6.98
	mea	2.50	4.05	5.44	6.72
$\delta_n = f_{n+1}/f_n$	sim	-	1.812	1.292	1.274
	mea	-	1.620	1.343	1.235
$R_{in}(\Omega)$	sim	38.46	51.72	47.66	53.96
	mea	35.01	52.37	53.89	49.26
$ S_{11} $ (dB)	sim	-25.02	-29.61	-24.67	-31.58
	mea	-22.97	-32.44	-31.57	-26.36
BW (-10 dB)	sim	400 MHz, 17.09%	770 MHz, 18.16%	300 MHz, 5.47%	960 MHz, 13.75%
	mea	198 MHz, 7.92%	300 MHz, 7.41%	255 MHz, 4.69%	383 MHz, 5.69%

(**sim**-simulated, **mea**-measured).

As presented in Table 2, adjacent frequency ratio δ_n of K_2 ABFH antenna is not equal to the fractal scale ratio σ_n of ABFL but varies from 1.274 to 1.812, because the four matched bands, as shown in Figure 17, are not identical modes engendered by the fractal iteration. However, ratio of f_4 to f_1 is just close to the fractal scale ratio σ . $f_1 = 2.34$ GHz, $f_2 = 4.24$ GHz, and $f_4 = 6.98$ GHz are axial modes induced by fractal's space-filling and self-similarity while $f_3 = 5.48$ GHz is off-axial mode yielded by fractal's impedance uniformity for multi-resonance, as shown in Figure 27. K_0 ABFH antenna also has off-axial mode at $f = 6.3$ GHz, but the impedance is far different from that of axial mode at $f = 3.5$ GHz. The fact manifests fractal's various functions in antenna design. The condition for axial mode operation is given in Equation (4) [26].

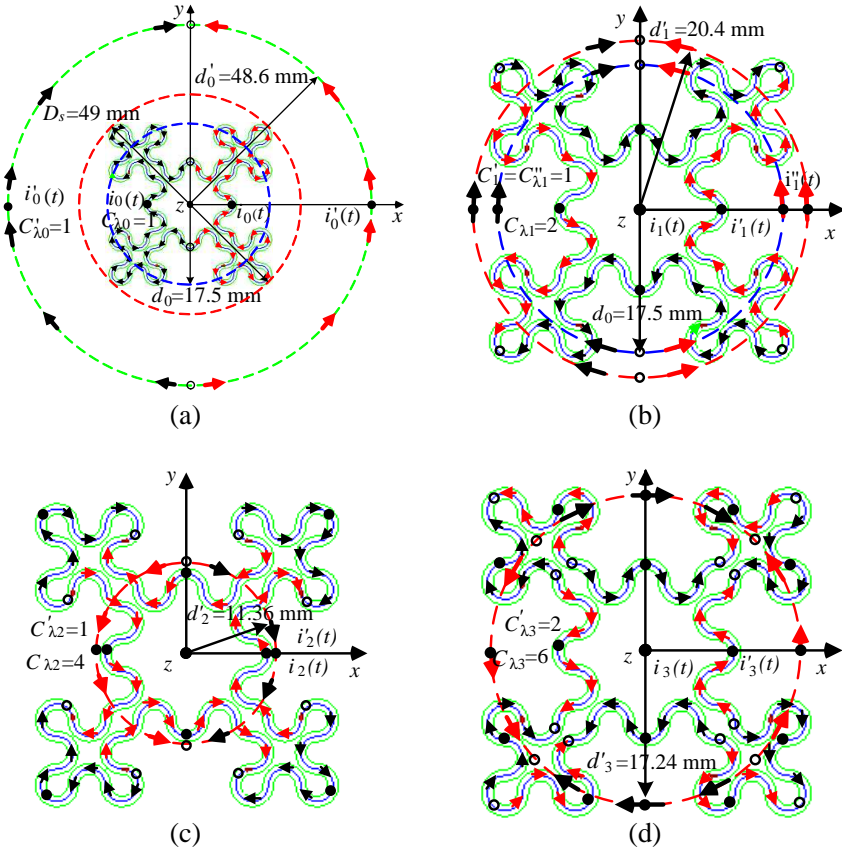
$$\frac{3}{4} \leq C_{\lambda_i} \leq \frac{4}{3} \Rightarrow \frac{C_{loop}}{\lambda_i} = \frac{2 \cdot \pi \cdot d'_i}{\frac{300}{f_i}} = \frac{2 \cdot \sqrt{\pi \cdot A_i}}{\frac{300}{f_i}} \approx 1.1, \quad (4)$$

where d'_i and A_i are equivalent radius and area of the loop respectively, and f_i is frequency in GHz, as shown in Figure 27. Considering

complexity, only qualitative analysis will be performed for the modes. Regardless of wave attenuation and turn-to-turn electromagnetic coupling, we can illustrate the equivalent current distributions of the bands with schematics, as shown in Figures 18(a)–(e). For $f_{1p} = 2.34$ GHz, $f_{2p} = 4.20$ GHz, $f_{3p} = 5.40$ GHz, and $f_{4p} = 7.34$ GHz, the equivalent loop radius is $d'_1 = 20.4$ mm, $d'_2 = 11.36$ mm, $d'_3 = 17.24$ mm, and $d'_4 = 8.62$ mm, respectively, as shown in Figures 18(b)–(e). Just like CHAs, K_2 ABFH operates in axial mode also with an equivalent loop circumference of about $1.1 \cdot \lambda$. According to Formula (4), $C_{\lambda_1} = 1.1$ corresponds to $f_{1p} \approx 3.0$ GHz for K_0 ABFH with radius $d_0 = 17.5$ mm. In contrast, K_2 ABFH operates in $C_{\lambda_1} = 1.1$ at $f_{1p} = 2.34$ GHz with a overall diameter of $D_s = 49$ mm, which means 16.73% size increase at fundamental resonant frequency, as depicted in Figure 18(b). In view of overall circumference of the ABFH loop, we can infer that there is another axial-mode band $f_0 \approx 1$ GHz ($C_{\lambda_0} = 1$). The equivalent loop radius is $d'_0 = 48.6$ mm, but diameter of the circum-circle is $D_s = 49$ mm, which means 49.59% of size shrinkage, as shown in Figure 18(a). However, this band's impedance is different from that of the four upper matched bands. Furthermore, the size of the ground plate is electrically small ($0.343 \cdot \lambda_0$), which will result in low gain. Therefore, the fundamental axial mode band f_0 is not presented.

As shown in Figures 18(a)–(e), currents of $f_{0p} = 1.0$ GHz, $f_{1p} = 2.34$ GHz, $f_{2p} = 4.20$ GHz, $f_{3p} = 5.40$ GHz, and $f_{4p} = 7.34$ GHz turn counter-clockwise and clockwise alternately on the ABFH loop with about $1 \cdot \lambda_0$, $2 \cdot \lambda_1$, $4 \cdot \lambda_2$, $6 \cdot \lambda_3$, and $8 \cdot \lambda_4$, respectively. The K_2 ABFH loop can be regards as a complex of four sub-loops in the corners (K_1 ABFH loop) and one main-loop in the center. Just like a CHA, $f_{0p} = 1.0$ GHz has a circularly symmetrical current distribution, which is equal in amplitude, identical in direction but opposite in phase, as depicted in Figure 18(a). Fields in $+Z$ -axis are superposed and strengthened. Phase progresses anti-clockwise along the winding direction of the helix. So, RHCP axial mode forms and high gain will be obtained with a larger ground disc. Current distributions of $f_{1p} = 2.34$ GHz on the sub-loops are identical but rotationally reverse, forming a four-element circular array. Such array effect for fractal antenna is firstly reported in [22]. In this way, current of opposite phase and orthogonal direction emerges in pairs on the loops. So, fields of these currents are cancelled with each other. Current on the main-loop turns counter-clockwise and clockwise alternately. However, it is electrical small without the current pairs, which are identical phase and orthogonally oriented, so axial fields cannot be cancelled mutually. Therefore, f_{1p} is RHCP axial mode with high gain, as

depicted in Figure 18(b). Current distributions of $f_{2p} = 4.20$ GHz on the sub-loops are identical and rotationally symmetrical, forming a four-element circular array. In this way, current of same phase and orthogonal direction emerges on the array in pairs. Furthermore, clockwise currents predominate on the sub-loops. Thus, the array operates in axial mode with LHCP. However, current on the main-loop is uniformly counter-clockwise with even amplitude. So, it behaves like an electrically small loop and yields axial nulls. Therefore, f_{2p} is LHCP axial mode with considerable gain, as depicted in Figure 18(c). Sense reversion of circular polarization is the most noteworthy peculiarity of K_2 ABFH antenna. Current distribution of $f_{3p} = 5.40$ GHz mainly resembles that of f_{1p} . The sub-loops also form a four-element array with identical but rotationally reverse current distributions, so the axial fields are cancelled. The main-loop also carries counter-clockwise and clockwise currents. However, it is electrically large with the current pairs, so axial fields are also cancelled. Therefore, f_{3p} is RHCP off-



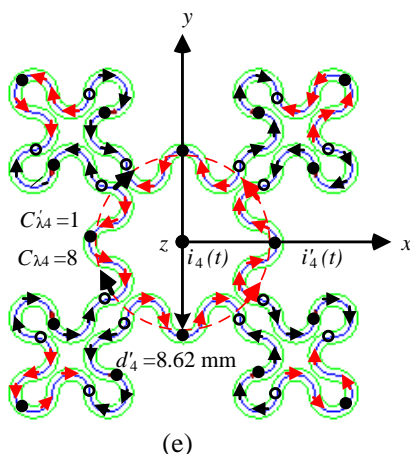


Figure 18. Bird's eye on current distribution of f_{ip} on the helix wire (green curve-outer boundary of helix wire, blue curve-schematic current path; red arrow-counterclockwise, black arrow-clockwise; black ring-null of current, black spot-peak of current; outer dash circle with arrow-equivalent circular loop of f_{ip}). (a) $f_{0p} = 1$ GHz (The overall K_2 ABFH loop, which carries two currents of circular symmetry, engenders RHCP axial mode, just as K_0 CHA dose). (b) $f_{1p} = 2.34$ GHz (Current distribution on the four sub-loops are identical but rotationally reverse, so axial fields are cancelled with each other. Main-loop is electrically small with counter-clockwise and clockwise current, so yields RHCP axial mode). (c) $f_{2p} = 4.20$ GHz (Current distribution on the four sub-loops are identical and rotationally symmetrical, so forming 4-element array with LHCP axial mode. Main-loop is electrically small with counter-clockwise current, so yields axial null. Therefore, overall is LHCP axial mode). (d) $f_{3p} = 5.40$ GHz (Current distribution on the four sub-loops are identical but rotationally reverse, so axial fields are cancelled with each other. Main-loop is electrically large with counter-clockwise and clockwise current, so yields RHCP off-axial mode). (e) $f_{4p} = 7.34$ GHz (Current distribution on the four sub-loops are identical and rotationally symmetrical, so forming 4-element array with RHCP axial mode. Main-loop is electrically large with counter-clockwise current, so yields RHCP axial mode. The overall gain is as high as 17.14 dBi).

axial mode with medium gain, as depicted in Figure 18(d). Current distribution of $f_{4p} = 7.34$ GHz resembles that of f_{3p} in the main. The sub-loops also form a four-element array with identical and rotationally symmetrical current distributions. The main-loop also carries counter-clockwise current. But it has large electrical size and the current pairs,

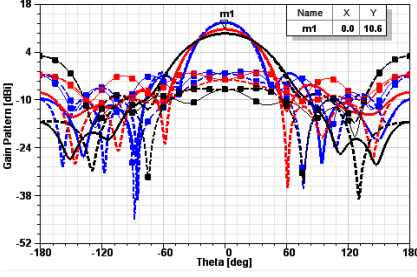


Figure 19. Gain patterns of K_i ABFH antenna at f_1 ($G = 10.6$ dBi; red-simulated of K_2 at $f_1 = 2.34$ GHz, black-measured of K_2 at $f_1 = 2.50$ GHz; blue-simulated of K_0 at $f_1 = 3.50$ GHz; solid- $\Phi = 0^\circ$ - XOZ , dash- $\Phi = 90^\circ$ - YOZ ; bare line-LHCP, marked line-RHCP).

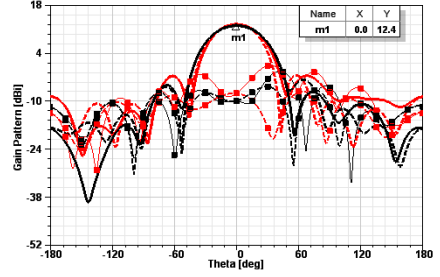


Figure 20. Gain patterns of K_2 ABFH antenna at f_2 ($G = 12.4$ dBi; red-simulated of K_2 at $f_2 = 4.20$ GHz, black-measured of K_2 at $f_2 = 4.05$ GHz; solid- $\Phi = 0^\circ$ - XOZ , dash- $\Phi = 90^\circ$ - YOZ ; bare line-LHCP, marked line-RHCP).

so yields RHCP axial mode. Furthermore, the sub-loop array also operates in RHCP axial mode. Therefore, f_{4p} is RHCP axial mode with unusual high gain, as depicted in Figure 18(e). In conclusion, main-loop has and sub-loop hasn't contribution to axial-mode of f_{1p} , main-loop hasn't and sub-loop has contribution to axial-mode of f_{2p} , neither main-loop nor sub-loop has contribution to axial-mode of f_{3p} , both main-loop and sub-loop have contribution to axial-mode of f_{4p} .

K_2 ABFH antenna achieves multiband multimode operation on trade-off of bandwidth decrease and size increment at fundamental band. However, its superiority and advantages over K_0 ABFH (CHA) are significant, such as axial-mode in multiband, dual senses of CP, usual high gain in upper band, small pitch angle. Fundamental bandwidth as wide as CHA is our major target in the next stage of study.

Hereunto, we can draw a significant conclusion that axial-mode wideband helix antenna can be made into multiband multimode with a special loop, which should form several relatively independent sub-loops surrounding considerable area. Obviously, **ML** is not such an ideal loop for the helix antenna.

Gain can be approximately calculated with the empirical formula in [28]:

$$G_{\max} (\text{dB}) = 10.25 + \zeta_1 \cdot \left(\frac{L'_T}{\lambda_p} \right) - \zeta_2 \cdot \left(\frac{L'_T}{\lambda_p} \right)^2 ;$$

$$L'_T = N \cdot \pi \cdot D' \cdot \tan \alpha = N \cdot \pi \cdot \left(2 \cdot \sqrt{\frac{A'}{\pi}} \right) \cdot \tan \alpha; \quad (5)$$

$$\zeta_1 = 1.22; \quad 0 < \zeta_2 < 0.1; \quad \lambda_{p|mm} = \frac{300}{f_p|GHz};$$

where ζ_1 and ζ_2 are constant coefficients; L'_T and N are total length and turns of the equivalent cylindrical helix respectively; D' and A'

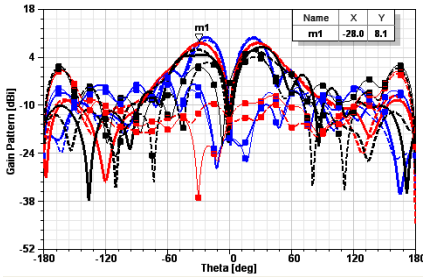


Figure 21. Gain patterns of K_i ABFH antenna at f_3 ($G = 8.1$ dBi; red-simulated of K_2 at $f_3 = 5.40$ GHz, black-measured of K_2 at $f_3 = 5.44$ GHz, blue-simulated of K_0 at $f_3 = 6.4$ GHz; solid- $\Phi = 0^\circ$ - XOZ , dash- $\Phi = 90^\circ$ - YOZ ; bare line-RHCP, marked line-LHCP).

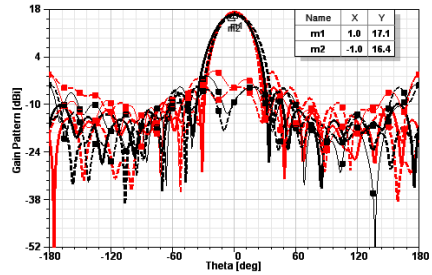


Figure 22. Gain patterns of K_2 ABFH antenna at f_4 ($G = 17.1$ dBi; red-simulated of K_2 at $f_4 = 7.34$ GHz, black-measured of K_2 at $f_4 = 6.72$ GHz; solid- $\Phi = 0^\circ$ - XOZ , dash- $\Phi = 90^\circ$ - YOZ ; bare line-RHCP, marked line-LHCP).

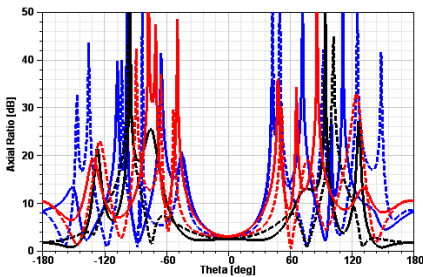


Figure 23. Axial ratio of K_i ABFH antenna at f_1 (red-simulated of K_2 at $f_1 = 2.34$ GHz, black-measured of K_2 at $f_1 = 2.50$ GHz; blue-simulated of K_0 at $f_1 = 3.50$ GHz; solid- $\Phi = 0^\circ$ - XOZ , dash- $\Phi = 90^\circ$ - YOZ).

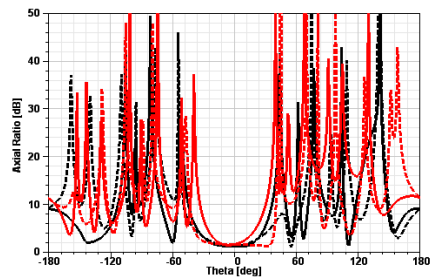


Figure 24. Axial ratio of K_2 ABFH antenna at f_2 (red-simulated of K_2 at $f_2 = 4.20$ GHz, black-measured of K_2 at $f_2 = 4.05$ GHz; solid- $\Phi = 0^\circ$ - XOZ , dash- $\Phi = 90^\circ$ - YOZ).

are diameter and area of the equivalent loop. As shown in Figure 27, when $f_p = 2.34$ GHz, 4.20 GHz, 5.40 GHz, and 7.34 GHz, $\zeta_2 = 0.1468$, 0.1185, 0.2121, and 0.0542, respectively. Besides band #1, high axial gain is also observed in bands #2, #3, and #4, as shown in Figure 27. In contrast, K_0 ABFH has high axial gain only in the fundamental band, also as shown in Figure 27. Gain patterns of the quad-bands in $\text{Phi} = 0^\circ$ and $\text{Phi} = 90^\circ$ cut-planes are illustrated in Figures 19–22. In these plots, solid and dash lines represent $\text{Phi} = 0^\circ$ (XOZ) and $\text{Phi} = 90^\circ$ (YOZ), respectively; red, black, and blue lines stand for simulated, measured K_2 ABFH, simulated K_0 ABFH in sequence, and bare and marked lines denotes co-polarization and cross-polarization component respectively. For distinct comparison, identical dynamic range (-52 dBi– $+18$ dBi) is chosen for these plots.

As shown in Figures 19–22, K_2 ABFH antenna has ideal axial radiation patterns, which are high gain dual-sensed circularly polarized (RHCP and LHCP) radiation at zenith ($+Z$ -axis) with quasi-symmetry in cut-planes $\text{Phi} = 0^\circ$ (XOZ) and $\text{Phi} = 90^\circ$ (YOZ). The peak gains of the quad-bands are $\mathbf{G} = 10.63$ dBi, 12.43 dBi, 8.13 dBi, and 17.14 dBi, which occur at $f_{1p} = 2.34$ GHz, $f_{2p} = 4.20$ GHz, $f_{3p} = 5.54$ GHz, and $f_{4p} = 7.34$ GHz, respectively. Higher gain can be obtained with the ground plate of larger dimension or reverse truncated conical-cup shape. The good polarization purity can be seen from spatial patterns of axial ratio, as shown in Figures 23–26, which degrade with Theta off the axial direction. Furthermore, beamwidth of axial ratio patterns is consistent with that of the gain patterns, which means good circular polarization within whole half-power beamwidth

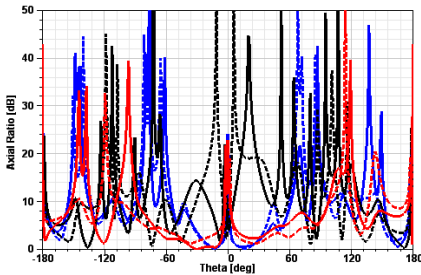


Figure 25. Axial ratio of K_i ABFH antenna at f_3 (red-simulated of K_2 at $f_3 = 5.40$ GHz, black-measured of K_2 at $f_3 = 5.44$ GHz, blue-simulated of K_0 at $f_3 = 6.4$ GHz; solid- $\text{Phi} = 0^\circ$ - XOZ , dash- $\text{Phi} = 90^\circ$ - YOZ).

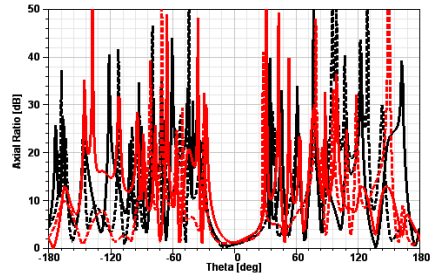


Figure 26. Axial ratio of K_2 ABFH antenna at f_4 (red-simulated of K_2 at $f_4 = 7.34$ GHz, black-measured of K_2 at $f_4 = 6.72$ GHz; solid- $\text{Phi} = 0^\circ$ - XOZ , dash- $\text{Phi} = 90^\circ$ - YOZ).

(HPBW). In addition, gain patterns have little discrepancy between the two cut-planes. Axial gain and front-to-back-ratio (FTBR) versus frequency in the quad-bands are shown in Figures 27 and 28. According to the formula in [24], axial AR in decibel (dB) can be calculated as below.

$$AR \text{ (dB)} = \left| L_\lambda \cdot \left(\sin \alpha - \frac{1}{p} \right) \right| = \sin \alpha \cdot \frac{(2 \cdot N + 1)}{2 \cdot N}; \tag{6}$$

$$p = \frac{L_\lambda}{S_\lambda + \frac{(2 \cdot N + 1)}{2 \cdot N}} = \frac{1}{\sin \alpha + \frac{(2 \cdot N + 1)}{2 \cdot N} \cdot \frac{\cos \alpha}{C_\lambda}},$$

where L_λ , S_λ , and C_λ are wire length, turn-to-turn spacing, and circumference of the helix in wavelength, respectively; $p = v/c$ is relative phase velocity; N and α have identical definition to the previous formulas. The smallest AR around $+Z$ -axis of the quad-bands is 3.23 dB, 1.72 dB, 0.11 dB ($\pm 30^\circ$), 0.35 dB in sequence, which is approximate to the theoretical value 0.056 from Formula (6). The

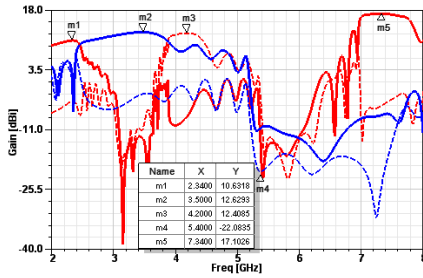


Figure 27. Simulated axial gain vs. f of K_i ABFH antenna (red- K_2 , blue- K_0 ; solid-RHCP, dash-LHCP).

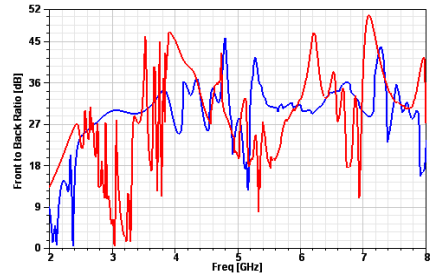


Figure 28. Simulated axial FTBR vs. f of K_i ABFH antenna (red- K_2 , blue- K_0).

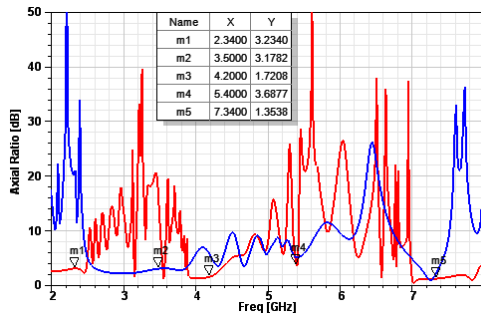


Figure 29. Simulated axial AR vs. f of K_i ABFH antenna (red- K_2 , blue- K_0).

Table 3. Radiation properties of K_2 ABFH antenna.

	Item	f_{1p}	f_{2p}	f_{3p}	f_{4p}
f_i (GHz)	sim	2.34	4.20	5.40	7.34
	mea	2.50	4.05	5.44	6.72
Gain (dBi)	sim	10.63	12.43	8.13	17.14
	mea	9.43	12.01	6.92	16.41
Pol	sim	RHCP	LHCP	RHCP	RHCP
	mea	RHCP	LHCP	RHCP	RHCP
AR (dB)	sim	3.23	1.72	0.11	1.35
	mea	2.68	1.41	1.64	0.91
HPWB (°)	sim	53.62,	47.72,	25.63,	31.56,
		52.26	46.56	23.67	32.94
	mea	59.41,	52.02,	24.45,	35.53,
BWFN (°)	sim	64.12,	48.06,	0, 120.21,	51.21
		58.03	46.11	0, 131.11	54.82
	mea	113.24,	52.92,	0, 96.21;	-39.92,
FSSL (dB)	sim	-1.78,	-2.09	0.46,	-7.49,
		-5.05	-1.62	-0.03	-7.11
	mea	-19.51,	-5.26,	-11.74,	-6.71,
		-9.45	-5.82	-11.22	-5.92

(sim-simulated, mea-measured; bold- XOZ , thin- YOZ).

axial AR versus frequency also manifests expected low value within the quad-bands, as depicted in Figure 29. The overall radiation characteristics of the quad-bands are presented in Table 3.

5. CONCLUSION

A novel circularly arched fractus named Arched Bow-shaped Fractal Curve (ABFC) is originally proposed. Then, a loop is constructed with four ABFCs and called Arched Bow-shaped Fractal Loop (ABFL). Fractal dimension D_F , physical scale ratio ζ_i , and fractal scale ratio σ_i , which dominate geometrical properties of ABFL, are thoroughly formulated. ABFL antenna peculiarly presents multiband multimode traits with resonance compression just when $K_i \geq 1$ ($i \geq 1$). Ratio of adjacent resonant frequencies $\delta_n(f_{n+1}/f_n)$ is found approximate to fractal scale ratio σ_i just when K_i is large and f_n high. The normal mode (Mode #3) is discovered pertinent to the loop area and circumference simultaneously, which diminishes and increases with K_i , respectively. So, the resonant frequency f_{ni} of K_i -iterated ($i \geq 1$) ABFL is higher than that of the initiator K_0 ABFL (circular loop) but

also decreases with K_i .

K_2 ABFL is then configured into a wire helix called Arched Bow-shaped Fractal Helix (ABFH) antenna with a copper disc ground. It can unprecedentedly operate in multiband of axial/off-axial mode with dual-sensed circular polarizations (CP) and high gain, which is almost impossible for a conventional helix antenna with any Euclidean geometry. Quad-bands ($|S_{11}| \leq -10$ dB) are obtained within 2 GHz–8 GHz. Compared with K_0 counterpart, K_2 ABFH has some negligible drawbacks, such as slight size increment and bandwidth shrinkage at fundamental resonance, and fabrication complexity. However, it has approximate fundamental band gain, higher upper-band gain, dual senses of circular polarization and more ideal axial ratio with smaller pitch angle ($\alpha = 3^\circ$), which mean significant height reduction ($\alpha = 10^\circ$ – 15°). This should be a big breakthrough for helix antenna since it was invented by J. D. Kraus early in 1946. The peculiar multiband multimode property has been theoretically analyzed. This trait can be attributed to the existence of the fractal boundary, which particularly encloses multiple equivalent loops with considerable areas. The unique properties makes K_2 ABFH antenna a very valuable candidate for multiband circularly polarized antennas, especially for space applications, such as spacecrafts communication, remote sensing, and telemetry, where reduction of quantity and weight of antennas are urgently wanted. It can also be configured into parabolic reflector's feed or large array for higher gain service like radar and radio astronomy. The problem of narrower bandwidth of fundamental resonance can be solved by some impedance matching techniques, using precise mould and accurate manufacture process, such as 3D printing technology.

ACKNOWLEDGMENT

The authors are grateful to Mr. Qian for his help in radiation patterns measurement. This work was supported by National Basic Research Program of China under Grant No. 2009CB320202.

APPENDIX A. MATHEMATICAL TRAITS OF ABFL AND ML

The total number of arc segments of ABFL and rectilinear segments of ML of successive iteration is:

$$N_{i+1} = 4 \cdot [(N_i + Q_i) + (i + 1) \cdot i^2 + 1] \\ (i = 0, 1, 2, \dots, n; \quad N_0 = 1; \quad Q_0 = 0, \quad Q_{i \geq 1} = 1) \quad (A1)$$

and

$$N'_{i+1} = 5 \cdot N'_i = 5^{i+1} \quad (i = -1, 0, 1, \dots, n) \quad (\text{A2})$$

respectively, where N_i and N'_i is the number of segments of K_i -iterated **ABFL** and **ML** separately. Radius d_i and total radian p_i of the arcs of **ABFL** of each iterative is:

$$d_i = \frac{d_0}{3^i} \quad (d_0 = 15.5 \text{ mm}; \quad i = 0, 1, 2, \dots, n) \quad (\text{A3})$$

and

$$p_{i+1} = 5 \cdot p_i = 5^{i+1} \cdot p_0; \quad (p_0 = 2 \cdot \pi; \quad i = 0, 1, 2, \dots, n) \quad (\text{A4})$$

From Equations (3) and (4), we can get overall arc length of ABFL of each iterative easily as follows:

$$l_{i+1} = p_{i+1} \cdot d_{i+1} = (5^{i+1} \cdot p_0) \cdot \frac{d_0}{3^{i+1}} = \left(\frac{5}{3}\right)^{i+1} \cdot (p_0 \cdot d_0); \quad (\text{A5})$$

$$\lim_{i \rightarrow \infty} l_{i+1} = +\infty \quad (i = 0, 1, 2, \dots, n)$$

The length ratio of middle indentation square to side segments of ML is e , as shown in Figures 1(b)–(d), so we obtain the minimum scale l_{0i} :

$$l_{0i} = \frac{L_0}{(2+e)^i} \quad (i = 0, 1, 2, \dots, n) \quad (\text{A6})$$

and total circumference l'_i :

$$\begin{aligned} l'_{i+1} &= \left(\frac{2+3 \cdot e}{2+e}\right) \cdot l'_i = \left(\frac{2+3 \cdot e}{2+e}\right)^i \cdot l'_0 \\ &= 4 \cdot \left(\frac{2+3 \cdot e}{2+e}\right)^{i+1} \cdot L_0 \quad (i = -1, 0, 1, \dots, n) \end{aligned} \quad (\text{A7})$$

of ML of K_i iteration.

Obviously, l_i and l'_i both grow infinitely during iterative process, but l_i increases more quickly. According to definition of box dimension [3, 9], we obtain fractal dimensions of ABFL and ML as follows:

$$\begin{aligned} D_F &= - \lim_{i \rightarrow \infty, \delta \rightarrow 0} \frac{\log M_{i+1}}{\log \delta_{i+1}} = - \lim_{i \rightarrow \infty, \delta \rightarrow 0} \frac{\log \left(\frac{l_{i+1}}{\delta_{i+1}}\right)}{\log \delta_{i+1}} \\ &= - \lim_{i \rightarrow \infty, \delta \rightarrow 0} \frac{\log \left[\left(\frac{5}{3}\right)^{i+1} \cdot (p_0 \cdot d_0)\right]}{\log \left(\frac{\pi}{2} \cdot \frac{d_0}{3^{i+1}}\right)} + 1 \\ &= 1.465 \quad (p_0 = 2 \cdot \pi, \quad d_0 = 15.5 \text{ mm}; \quad i = 0, 1, \dots, n) \end{aligned} \quad (\text{A8})$$

$$\begin{aligned}
 D'_F &= - \lim_{i \rightarrow \infty, \delta \rightarrow 0} \frac{\log M'_{i+1}}{\log \delta'_{i+1}} = - \lim_{i \rightarrow \infty, \delta \rightarrow 0} \frac{\log \left(\frac{l'_{i+1}}{e \cdot l_{0i+1}} \right)}{\log (e \cdot l_{0i+1})} \\
 &= - \lim_{i \rightarrow \infty, \delta \rightarrow 0} \frac{\log [4 \cdot e^{-1} \cdot (2+3 \cdot e)^{i+1}]}{\log \left[\frac{e \cdot L_0}{(2+e)^{i+1}} \right]} = 1 < \frac{\log(2+3 \cdot e)}{\log(2+e)} < 1.465 \\
 &\quad (e \in [0, 1], L_0 = 2 \cdot d_0; i = 0, 1, \dots, n), \quad (A9)
 \end{aligned}$$

where M_i, M'_i is equivalent segment numbers of the i th-iterated ABFL and ML measured with unit scale of $\pi/4$ radian and $e \cdot l_{0i}$ respectively. Then, we obtain physical scale ratios ζ_i :

$$\zeta_{i+1} = \lim_{i \rightarrow \infty} \frac{M_{i+1} \cdot \delta_{i+1}}{M_i \cdot \delta_i} = \frac{l_{i+1}}{l_i} = \frac{\left(\frac{5}{3}\right)^{i+1} \cdot (p_0 \cdot d_0)}{\left(\frac{5}{3}\right)^i \cdot (p_0 \cdot d_0)} = \frac{5}{3} \approx 1.667 \quad (A10)$$

$$\zeta'_{i+1} = \lim_{i \rightarrow \infty} \frac{M'_{i+1} \cdot \delta'_{i+1}}{M'_i \cdot \delta'_i} = \frac{l'_{i+1}}{l'_i} = 1 < \frac{2+3 \cdot e}{2+e} < 1.667 \quad (e \in [0, 1]), \quad (A11)$$

and fractal scale ratios σ_i :

$$\lim_{i \rightarrow \infty} \sigma_i = \lim_{i \rightarrow \infty} \frac{r^i}{r^{i-1}} = \lim_{i \rightarrow \infty} \frac{[(3^i - 1) \cdot \sqrt{2} + 1] \cdot \frac{d_0}{3^i}}{[(3^{i-1} - 1) \cdot \sqrt{2} + 1] \cdot \frac{d_0}{3^{i-1}}} \approx 3 \quad (i = 1, 2, \dots, n) \quad (A12)$$

$$\lim_{i \rightarrow \infty} \sigma'_i = \lim_{i \rightarrow \infty} \frac{l_{0i}}{l_{0i-1}} = 2 < 2+e < 3 \quad (e \in [0, 1]; i = 1, 2, \dots, n) \quad (A13)$$

of ABFL and ML.

where r^i is diagonal radii of the i th-iterated ABFL. As shown in formula (8)–(13), fractal dimension D_F , physical scale ratio ζ_i , and fractal scale ratio σ_i of the two fractal loops are both all different. This circumstance is very frequent with almost all fractals. And this property might be intimately associated with the antenna's performance. Besides the quantities shown above, another crucial parameter for ABFL and ML is area A_i , which is:

$$\begin{aligned}
 \lim_{i \rightarrow +\infty} A_i &= 4 \cdot d_0^2 - (b_i - \pi) \cdot d_i^2 \\
 &= 4 \cdot d_0^2 - \left(\frac{\sum_{k=0}^{2 \cdot i} a_k \cdot 3^k}{3^{2 \cdot i}} - \frac{\pi}{3^{2 \cdot i}} \right) \cdot d_0^2 \\
 &= \left\{ 4 - \left[\frac{\beta \cdot (1 - 3^{1+2 \cdot i})}{3^{2 \cdot i}} - \frac{\pi}{3^{2 \cdot i}} \right] \right\} \cdot d_0^2
 \end{aligned}$$

$$\begin{aligned}
&= \left[4 - \beta \cdot \frac{3}{2} + \frac{(0.5 \cdot \beta + \pi)}{3^{2 \cdot i}} \right] \cdot d_0^2 \approx \left(4 - \beta \cdot \frac{3}{2} \right) \cdot d_0^2 \\
0 &= \left(4 - \frac{8}{3} \cdot \frac{3}{2} \right) \cdot d_0^2 \leq A_i \leq \left(4 - 1 \cdot \frac{3}{2} \right) \cdot d_0^2 = 2.5 \cdot d_0^2 \\
&\quad \left(\beta \in \Phi = \left[1, \frac{8}{3} \right] \right) \quad (\text{A14})
\end{aligned}$$

and

$$\lim_{i \rightarrow +\infty} A'_i = \left\{ 1 - 4 \cdot \sum_{j=0}^{i-1} \left[\frac{2 + 3 \cdot e^2}{(2 + e)^2} \right]^j \cdot \left(\frac{e}{2 + e} \right)^2 \right\} \cdot A'_0$$

$$(A'_0 = L_0^2; \quad e \in [0, 1]; \quad i = 1, 2 \dots n), \quad (\text{A15})$$

respectively. In Equation (A14), when $i = 0$, $b_0 = a_0 = 4$; $i = 1$, $b_1 = 20$, $a_2 = 1$, $a_1 = 3$, $a_0 = 2$; $i = 2$, $b_2 = 196$, $a_4 = 1$, $a_3 = a_2 = 3$, $a_1 = 2$, $a_0 = 1$; $i = 3$, $b_3 = 1844$, $a_6 = 2$, $a_5 = a_4 = a_3 = 1$, $a_2 = 3$, $a_1 = a_0 = 2$. There is an approximate expression for terms of series b_i ($i = 0, 1, \dots, n$): $b_{i+2} = 9 \cdot b_{i+1} + 4 \cdot b_i$, which tends to grow exponentially.

REFERENCES

1. Cohen, N., "Fractal antennas: Part 1," *Communications Quarterly*, 7–22, Aug. 1995.
2. Cohen, N., "Fractal antenna applications in wireless telecommunications," *IEEE Electronics Industries Forum of New England*, 43–49, May 1997.
3. Mandelbrot, B. B., *The Fractal Geometry of Nature*, 2nd Edition, W. H. Freeman, New York, 1983.
4. Werner, D. H., R. L. Haup, and P. L. Werner, "Fractal antenna engineering: The theory and design of fractal antenna arrays," *IEEE Antennas and Propagation Magazine*, Vol. 41, No. 5, 37–58, Oct. 1999.
5. Gianvitorio, J. and Y. Rahmat, "Fractal antennas: A novel antenna miniaturization technique and applications," *IEEE Antennas and Propagation Magazine*, Vol. 44, No. 1, 20–36, Feb. 2002.
6. Anguera, J., C. Puente, C. Borja, and J. Soler, "Fractal-shaped antennas: A review," *Wiley Encyclopedia of RF and Microwave Engineering*, Vol. 2, 1620–1635, Apr. 2005.

7. Liu, Y., S. Gong, and D. Fu, "The advances in development of fractal antennas," *Chinese Journal of Radio Science*, Vol. 17, No. 1, Feb. 2002.
8. Vinoy, K. J., "Fractal shaped antenna elements for wide and multi band wireless applications," The Graduate School College of Engineering, The Pennsylvania State University, Aug. 2002.
9. Falconer, K., *Fractal Geometry: Mathematical Foundations and Applications*, 2nd Edition, John Wiley & Son, Inc., New York, 2003.
10. Baliarda, C. P., J. Romeu, and A. Cardama, "The Koch monopole: A small fractal antenna," *IEEE Trans. on Antennas and Propaga.*, Vol. 48, No. 11, 1773–1781, Nov. 2000.
11. Li, D. T. and J. F. Mao, "A Koch-like sided bow-tie fractal dipole antenna," *IEEE Trans. on Antennas and Propaga.*, Vol. 60, No. 5, 40–49, May 2012.
12. Mirzapour, B. and H. R. Hassani, "Size reduction and bandwidth enhancement of snowflake fractal antenna," *IET Microwave Antennas Propag.*, Vol. 2, No. 2, 180–187, Mar. 2008.
13. Mahatthanajatuphat, C., S. Saleekaw, and P. Akkaraekthalin, "A rhombic patch monopole antenna with modified Minkowski fractal geometry for UMTS, WLAN, and mobile WiMAX application," *Progress In Electromagnetics Research*, Vol. 89, 57–74, 2009.
14. Gonzalez-Arbesu, J. M., S. Blanch, and J. Romeu, "The Hilbert curve as a small self-resonant monopole from a practical point of view," *Microwave and Optical Technology Letters*, Vol. 39, No. 1, 45–49, Oct. 2003.
15. Zhu, J., A. Hoorfar, and N. Engheta, "Bandwidth, cross polarization and feed-point characteristics of matched Hilbert antennas," *IEEE Antennas and Wireless Propagation Letters*, Vol. 2, No. 1, 2–5, Jan. 2003.
16. Werner, D. H., W. Kuhirun, and P. L. Werner, "The Peano-Gosper fractal array," *IEEE Trans. on Antennas and Propaga.*, Vol. 51, No. 8, 2063–2072, Aug. 2003.
17. Zhu, J., A. Hoorfar, and N. Engheta, "Peano antennas," *IEEE Antennas and Wireless Propagation Letters*, Vol. 3, 71–74, Jan. 2004.
18. Puente, C., J. Romeu, R. Pous, and A. Cardama, "On the behavior of the Sierpinski multiband fractal antenna," *IEEE Trans. on Antennas and Propaga.*, Vol. 46, 517–524, Apr. 1998.
19. Oraizi, H. and S. Hedayati, "Miniaturized UWB monopole microstrip antenna design by the combination of Giuseppe Peano

- and Sierpinski carpet fractals,” *IEEE Antennas and Wireless Propagation Letters*, Vol. 10, 67–70, 2011.
20. Kumar, R. and P. N. Chaubey, “On the design of inscribed pentagonal-cut fractal antenna for ultra-wideband applications,” *Microwave and Optical Technology Letters*, Vol. 53, No. 12, Dec. 2011.
 21. Li, D. T. and J. F. Mao, “Koch-like sided Sierpinski gasket multifractal dipole antenna,” *Progress In Electromagnetics Research*, Vol. 26, 399–427, 2012.
 22. Li, D. T. and J. F. Mao, “Sierpinskized Koch-like sided multifractal dipole antenna,” *Progress In Electromagnetics Research*, Vol. 13, 207–224, 2012.
 23. Kraus, J. D. and R. J. Marhefka, *Antennas: For All Application*, 3rd Edition, McGraw-Hill, Nov. 2001.
 24. Kraus, J. D., “The helical antenna,” *Proceedings of the IRE*, Vol. 37, No. 3, 263–272, Mar. 1949.
 25. Kraus, J. D. and J. C. Williamson, “Characteristics of helical antennas radiating in the axial mode,” *Journal of Applied Physics*, Vol. 19, No. 1, 87–96, Jan. 1948.
 26. Yousaf, J., M. Amin, and S. Iqbal, “Design of circularly polarized omnidirectional bifilar helix antennas with optimum wide axial ratio beamwidth,” *Progress In Electromagnetics Research C*, Vol. 39, 119–132, 2013.
 27. Amin, M., J. Yousaf, and M. K. Amin, “Terrestrial mode quadrifilar helix antenna,” *Progress In Electromagnetics Research Letters*, Vol. 27, 179–187, 2011.
 28. Weeratumanoon, E., “Helical antennas with truncated spherical geometry,” The Virginia Polytechnic Institute and State University, Blacksburg, Virginia, Jan. 27, 2000.
 29. Gharibi, H. and F. H. Kashani, “Design of a wideband monopulse antenna using four conical helix antennas,” *Progress In Electromagnetics Research Letters*, Vol. 29, 25–33, 2012.
 30. Best, S. R., “The fractal loop antenna: A comparison of fractal and non-fractal geometries,” *IEEE Antennas and Propagation Society International Symposium*, Vol. 3, 146–149, Jul. 2001.